Size effect on multiferroicity of GdMn$_2$O$_5$ nanorods

Yang-Hsiang Tung [a], Yi-Jung Chen [a], Chun-Chuen Yang [a,*], Cheng-Yu Weng [a],
Yen-Kai Huang [a], Yang-Yuan Chen [b], Maw-Kuen Wu [b]

[a] Department of Physics, Chung Yuan Christian University, 200, Chung Pei Rd., Chung Li 32023, Taiwan
[b] Institute of Physics, Academia Sinica, 128 Sec. 2, Academia Rd., Nankang, Taipei 11529, Taiwan

A B S T R A C T

Four GdMn$_2$O$_5$ nanorod samples of various axial lengths ($\langle L_C \rangle$) along the c axis were synthesized. The antiferromagnetic and ferroelectric ordering disappeared as $\langle L_C \rangle$ decreased to 66 and 55 nm. Various ferroic critical sizes were observed for the two types of domain sizes. Between T = 18 and 26 K, a charge ordering X-ray diffraction peak appeared at $\langle L_C \rangle$ = 79 nm. This peak was associated with structural distortion and axial length. The broken multiferroicity of the GdMn$_2$O$_5$ nanorods limits their practical application. For applications in memory devices, the estimated maximal capacity is approximately 650 Gbits/in^2.

1. Introduction

Multiferroics are materials that exhibit two or more ferroic behaviors, including magnetoelectricity, piezoelectricity, and piezomagneticity [1–5]. Multiferroics can be used for fabricating next-generation memory storage devices [5]. Various types of memory devices have been developed using BiFeO$_3$, RMnO$_3$, and RMn$_2$O$_5$ compounds, where R stands for rare earth [6–8]. For example, Zavaliche et al. demonstrated an electrically assisted magnetic recording method for the multiferroic nanostructure of BiFeO$_3$–CoFe$_2$O$_4$ [9]. Bibes and Barthélémy designed a novel structure called "MERAM" using magnetoelectric materials for use in memory devices [10]. Yu-Ting Tsai et al. reported high-performance resistance-switching Pt/DyMn$_2$O$_5$/TiN memory devices [8]. These studies indicate the feasibility of designing memory devices using multiferroic materials. Such devices exhibit high stackability and rapid electronic access. However, the physical limitations of multiferroic materials should be clarified. Typical magnets lose their permanent magnetism when their size is smaller than the superparamagnetic limit [11]. This effect is also evident in multiferroics, which places a functional size limit on their applicability. In sandwich structures, the information in each bit is preserved magnetically and accessed electronically [10]. Any improper response of the magnetic or electric signal causes a loss of valuable information. Therefore, the determination of the magnetic and electric critical sizes is crucial for practical applications. Another consideration is driven by the need for the recording density of the multiferroic designs to be comparable with those of current designs. The commercial perpendicular magnetic recording (PMR) technique has improved hard disk recording density by as much as 500–600 Gbits/in^2 and facilitated the fabrication of magnetic recording devices of sizes close to the superparamagnetic limit [12]. In contrast to planar designs, the use of three-dimensional and stackable designs can overcome the size limitation. RMn$_2$O$_5$ compounds are multiferroic material with magnetoelectric properties [5,13–15]. Due to their electronic configuration and among the rare earth elements, gadolinium exhibits the largest magnetic moment difference between neighboring elements (Eu = 0 μ_B, Gd = 7.94 μ_B, and Tb = 9.72 μ_B). This large difference implies that any variation in valence electrons causes large changes in magnetic moment, especially in small-sized samples that have large bounding defects at their surfaces. Furthermore, although magnetic or electric ordering can be induced using

---

* Corresponding author.
   E-mail address: chunchuenyang@cycu.edu.tw (C.-C. Yang).

an external field through the magnetoelectric effect, in practice, both orderings must occur spontaneously and simultaneously to preserve information [10]. This study determined the maximum recording density that is set by the critical size associated with the multiferroicity of GdMn$_2$O$_5$ nanorods. The importance of the size effect in structural, magnetic, and electric properties was also uncovered.

2. Sample preparation

GdMn$_2$O$_5$ nanorods were synthesized using a hydrothermal method [16,17]. The obtained powder was divided into five parts and sintered in an electrical furnace at annealing temperatures (T$_a$) of 400, 600, 800, 1000, and 1200 °C. For comparison, a bulk sample was also prepared using the conventional solid-state reaction method.

3. Experiment

3.1. X-ray diffraction

The composition and purity of the sample were determined using a Philips X'pert powder X-ray diffractometer at a Cu-Kα wavelength. The diffraction patterns were analyzed using the General Structure Analysis System (GSAS) program according to the Rietveld refinement method [18]. Fig. 1(a) presents the obtained patterns, which reveal that the nanorods maintain the same crystal structure as that of the bulk when the annealing temperatures are equal or less than 1000 °C. Structural refinement revealed that the GdMn$_2$O$_5$ nanorods and bulk samples exhibited orthorhombic *Pbam* symmetry [19,20]. As T$_a$ increased to 1200 °C, GdMn$_2$O$_5$ decomposed into two major compounds, namely GdMnO$_3$ and Mn$_3$O$_4$, at a molar ratio of approximately 71% to 29% [19]. The size of the nanorods was correlated with the annealing temperature. The full width half maximum (FWHM) of the {112} single peak at 2θ = 35.6° decreased with increasing of T$_a$, which indicated that the size of the samples increased with annealing temperature.

3.2. Transmission electron microscopy images

To quantify the sizes of the four types of single-phase GdMn$_2$O$_5$ nanorods, JEOL JEM-2100 field emission transmission electron microscopy (FE-TEM) and selection area electron diffraction (SAED) were performed to determine the axial/radial lengths and their directions [21]. Fig. 1(b) displays the results of the T$_a$ = 1000 °C sample. The FE-TEM images and SAED patterns reveal that the *c* axis
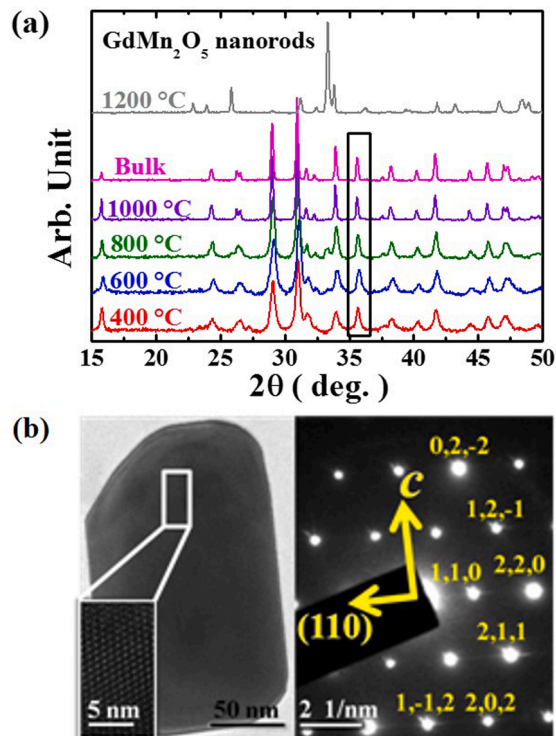
Fig. 1. (a) X-ray diffraction patterns of GdMn$_2$O$_5$ bulk and nanorods at various annealing temperatures (T$_a$) of 400, 600, 800, 1000, and 1200 °C. (b) Transmission electron microscopy (TEM) image of $\langle L_C \rangle$ = 198 nm GdMn$_2$O$_5$ nanorods. Inset image displays the selected area electron diffraction (SAED) patterns and high-resolution electron microscopic images.

of the crystal is parallel to the axial direction of the nanorods [16]. This phenomenon was also observed in nanorods annealed at $T_a =$ 400, 600, 800, and 1000 °C. A similar phenomenon was not observed for the radial direction with a specified orientation. By contrast, the mean measured values of the axial length (error bar) × radial length (error bar) for the samples with $T_a =$ 400, 600, 800, and 1000 °C were 55 (10) nm × 26 (7) nm, 66 (10) nm × 31 (6) nm, 79 (12) nm × 31 (5) nm, and 198 (43) nm × 99 (26) nm, respectively. For brevity and to provide crystal orientation, the samples are referred to by their mean axial lengths, $\langle L_C \rangle$, rather than their T_a.

3.3. Magnetic properties

AC magnetic susceptibility measurements were performed using a quantum-design physical property measurement system (PPMS) from Quantum Design with the standard setup. The sample was subjected to a weak driving AC magnetic field at 10 Oe with a frequency of 10^3 Hz (f_m). Fig. 2(a) displays the collected temperature profiles of the in-phase component χ' of the bulk, at $\langle L_C \rangle = 198$, 79, 66, and 55 nm. The χ'–T curve of the bulk reveals a magnetic susceptibility increase at 43 K (T*). This increase is associated with the starting of the incommensurate antiferromagnetic ordering of Mn ions [20]. Simultaneously, a small distinct feature that is related to the transition from incommensurate to commensurate antiferromagnetic ordering was observed at 41.5 K (T_{CAF}) [20]. For samples with $\langle L_C \rangle = 198$ and 79 nm, the values of T* and T_{CAF} were 2 and 1 K lower, respectively, than those of the bulk. By contrast, no antiferromagnetic (AFM) peaks were observed when $\langle L_C \rangle$ was 66 and 55 nm. When above 80 K, all samples were in the paramagnetic phase. The effective magnetic moment (μ_{eff}) and Néel temperature (T_N) in Fig. 2(b) were obtained by curve fitting using the Curie–Weiss law. Both μ_{eff} and T_N reduced with decreasing $\langle L_C \rangle$. An abrupt decrease in both parameters occurred between $\langle L_C \rangle = 79$ and 66 nm, which corresponded with the disappearance of the AFM peak in Fig. 2(a). As $\langle L_C \rangle$ decreased, both T* and T_N shifted to lower temperatures, which implied that the size effect weakened the magnetic coupling between Mn ions. Both figures reveal that the critical length of magnetic ordering was between 66 and 79 nm. Notably, the radial lengths of $\langle L_C \rangle = 55$, 66, and 79 nm were all near 30 nm to within the statistical error, which indicated that the critical length of AFM magnetic ordering may not be obviously correlated with the radial length but governed by the correlation length along the c axis of the crystal ($<L_C>$ length).

3.4. Dielectric properties

The effects of the size on the dielectric properties of the nanorods were investigated. Samples were packed, wired, and placed in a closed-cycle refrigerator with precise temperature maintenance using a Lakeshore 325 temperature controller. An Agilent E4980A LCR meter was used to measure the capacitance of the samples in excited AC electric fields of various frequencies (f_e). The in-phase relative dielectric constant ε' was calculated from the measured capacitance. Here, the porosity (P) of each sample was between 33% and 35%, which is the contribution of the vacuum. Fig. 3(a) illustrates the ε' of the bulk for the samples with $\langle L_C \rangle = 79$, 66, and 55 nm at $f_e = 10^3$

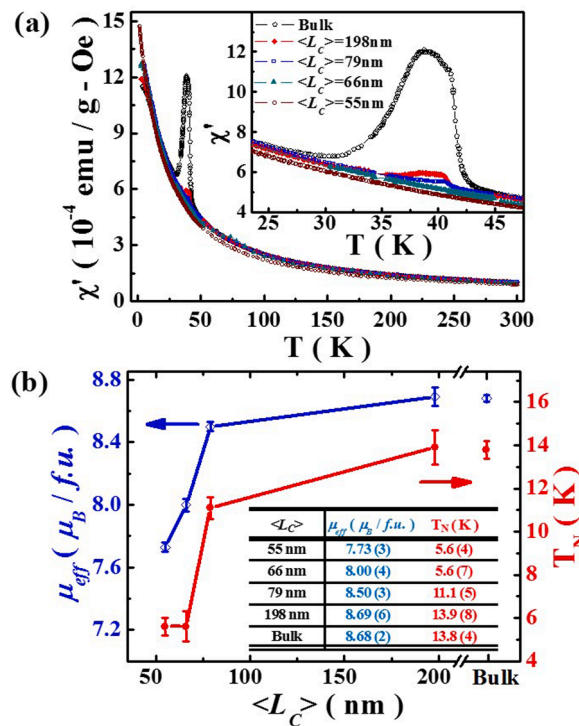Fig. 2. (a) χ'–T curves of bulk, $<L_C> = 198$, 79, 66, and 55 nm nanorods. (b) Fitted effective magnetic moment μ_{eff} and Néel temperature T_N of four nanorod and one bulk samples.

Hz. The corresponding ferroelectric (FE) ordering temperatures (T_c) were approximately 38, 42, 43 K, and unavailable, respectively. Here, T_c increased as the size became larger than 55 nm. Moreover, the saturated dielectric constant (ε_s') of FE ordering at approximately 14 K decreased as the size decreased. The critical size of FE ordering was 55 nm, which is smaller than the 66 nm of AFM. This observation implies that the FE domain is smaller than that of AFM and can hold finite FE ordering at 66 nm. Otherwise, the FE domain is sensitive to the frequency of the AC electric field. Fig. 3(b), (c), and (d) display the results of $\langle L_C \rangle$ = 79, 66, and 55 nm samples at frequencies from 10^3 to 10^6 Hz. The ε_s' of all three samples decreased with increasing frequency. Compared with the reduction of ε' (i. e., $\Delta\varepsilon'$) at $f_e = 10^6$ Hz between the samples with the $\langle L_C \rangle$ of 79 and 66 nm, the $\Delta\varepsilon'$ value between 14 (ε_s') and 45 K (above T_c) of the sample with $\langle L_C \rangle$ = 79 nm was finite. By contrast, the $\Delta\varepsilon'$ of the sample with $\langle L_C \rangle$ = 66 nm was almost zero. This finding implies a correlation between frequency and axial length in the nanorods.
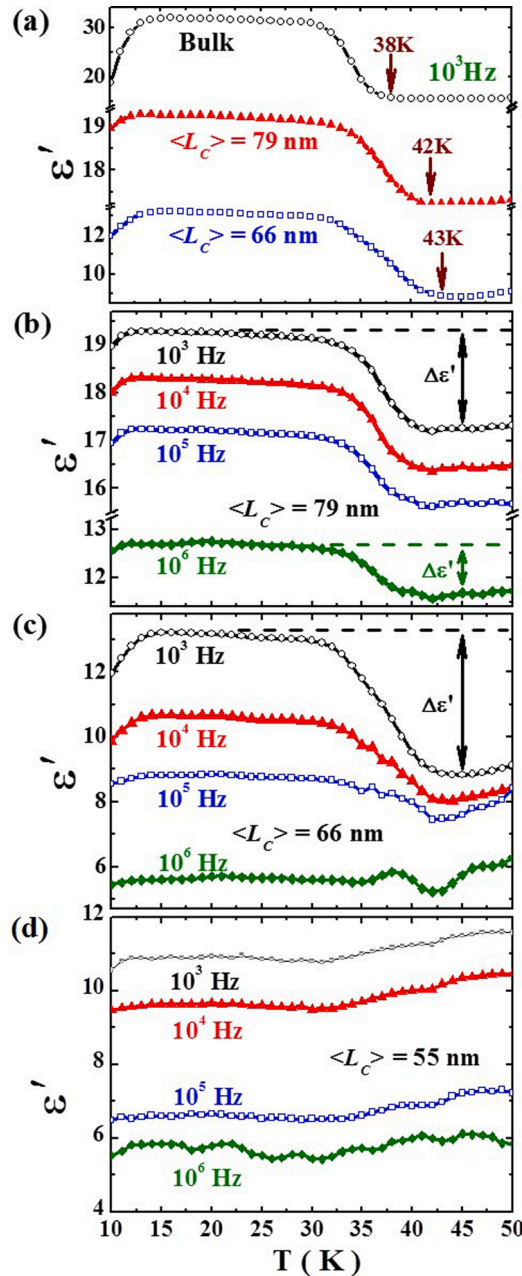

Fig. 3. (a) Measured relative dielectric constants of bulk for $<L_C>$= 79, 66, and 55 nm samples excited at an AC frequency of 10^3 Hz. Samples with $\langle L_C \rangle$ = (b) 79 nm, (c) 66 nm, and (d) 55 nm at various AC frequencies.

4. Discussion

Several studies have reported that the polarization of the AFM domain in the multiferroic materials is governed by FE polarizations, which originate from the coupling between FE and AFM domain walls (DWs) and result in excellent tunability by the external electric field [22–24]. By contrast, some AFM domains located at structural defects do not easily change their polarization and result in frozen coupled FE DWs. This behavior results in bad response at higher frequencies. Furthermore, the structural defects typically occur at sample surfaces (which have abnormal bonds), and these defects are especially critical in nanorods with a large surface-to-volume ratio. Therefore, materials with smaller $\langle L_C \rangle$ exhibit lower ε' than materials with larger $\langle L_C \rangle$ do (Fig. 3[a]). The difference between the values of μ_{eff} for the nanorods and the bulk can be used to estimate the portion of AFM DWs located at structural defects. Magnetic moments that are at the surface may not respond to an excited AC magnetic field and may have a lower contribution to μ_{eff}. The reduction of μ_{eff} of the bulk by this effect can be neglected so that the μ_{eff} of the bulk (μ_{eff}^{bulk}) to be used as a standard for comparison. Here, the ratio of the surface defects of $\langle L_C \rangle = 66$ to 79 nm was estimated to be $(\mu_{eff}^{bulk} - \mu_{eff}^{66\,nm}) / (\mu_{eff}^{bulk} - \mu_{eff}^{79\,nm}) = 0.68 \pm 0.06/0.18 \pm 0.05 = 3.8 \pm 1.9$ (from the table in Fig. 2(b)), which is close to the reduction ratio of $(\Delta\varepsilon'^{66\,nm}_{1KHz} - \Delta\varepsilon'^{66\,nm}_{1MHz})/(\Delta\varepsilon'^{79\,nm}_{1KHz} - \Delta\varepsilon'^{79\,nm}_{1MHz}) = 4.3/1 = 4.3$ (from Fig. 3(b) and (c)). These calculations verified the previous inference and reveal the consistency between magnetic and electric properties.

The mechanism of magnetoelectric coupling involves simultaneous magnetic and electric ordering and is governed by structural distortions [20]. These distortions can be attributed to the size effect. To investigate the relationship between structural distortions and the size effect, in situ X-ray diffraction (XRD) was performed on $\langle L_C \rangle = 66$ and 79 nm samples, whose lengths were close to the critical limits, at various temperatures from 10 to 55 K at intervals of 5 K [25]. Fig. 4(a) displays the results of the refinement of $\langle L_C \rangle = 79$ nm at 25 K. An additional peak was observed at $2\theta = 27.3°$ This peak was not indexed by the orthorhombic *Pbam* symmetry. Many space groups, including Pb2$_1$m symmetry, have been tested in the refinement, but no group has matched the peak [20,26]. The $\langle L_C \rangle = 66$ nm sample did not exhibit this peak in the temperatures of interest. To trace the evolution of the peak, experiments were conducted again between 15 and 30 K at 1 K intervals with $2\theta = 25°–30°$ Fig. 4(b) displays the temperature profile of the $\langle L_C \rangle = 79$ nm sample, which
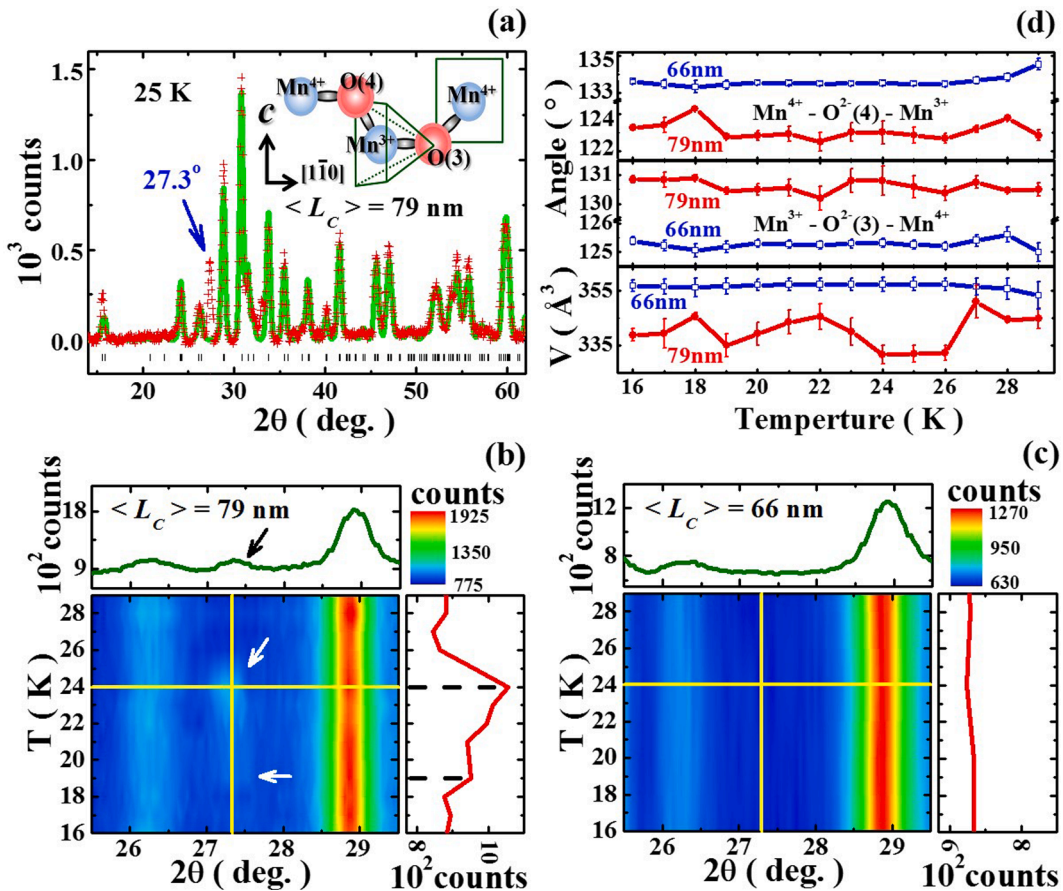

Fig. 4. (a) Refinement results from X-ray diffraction pattern for $\langle L_C \rangle = 79$ nm at 25 K. Observed (red crosses) and calculated (green solid line) values with estimated peak positions (black dash) are presented. Diffraction patterns obtained at various temperatures for (b) $\langle L_C \rangle = 79$ nm and (c) $\langle L_C \rangle = 66$ nm nanorods are also plotted. (d) Refined cell volume and Mn^{3+}-O-Mn^{4+} angles of $\langle L_C \rangle = 79$ nm and $\langle L_C \rangle = 66$ nm.

exhibited an additional peak at approximately 18 K and suddenly disappeared at 27 K. Two local maxima were observed at 19 and 24 K. No similar observations were made for the $\langle L_C \rangle = 66$ nm sample in Fig. 4(c). Fig. 4(d) displays the cell volume and the Mn^{3+}-O-Mn^{4+} bond angles of both samples. The variation of the $\langle L_C \rangle = 79$ nm sample was larger than that of the $\langle L_C \rangle = 66$ nm sample. In Fig. 4(b), two local cell volume minima are illustrated to be associated with two local maxima of the additional peak. Moreover, the Mn^{4+}-O^{2-}(4)-Mn^{3+}-O^{2-}(3)-Mn^{4+} chain is roughly extended in the $[1\bar{1}0]$ direction and confined by the radial length. The inset in Fig. 4 (a) displays the Mn and O positions at the pyramid and the plane through the middle of an octahedron. The radial lengths of the two samples were almost equal, which implied that the only differences between the two samples were the mean axial length. This study revealed that increasing the axial length reduced the cell volume and created distortions inside the unit cell, which resulted in periodic charge ordering. The charge ordering peak at 27.3° can be indexed as {2 1 ½}, and its intensity varies with the extent of distortion. Giovannetti et al. reported theoretical calculations concerning similar phenomena that involved the transfer of charges between manganese and oxygen ions and proposed a relationship between distortion and bond lengths [26].

5. Conclusion

The magnetic, electric, and structural properties of nanorods with various $\langle L_C \rangle$ were investigated. Multiferroicity is broken by the disappearance of AFM ordering when $\langle L_C \rangle$ is 66 nm. The FE ordering was suppressed when $\langle L_C \rangle$ is 55 nm. Smaller $\langle L_C \rangle$ result in larger surface defects to volume ratio and hinder the motion of FE DWs. Therefore, ε' is decreases as size decreases and results in a bad response to high frequencies. XRD experiments on the $\langle L_C \rangle = 79$ nm sample between 18 and 26 K yielded a charge ordering peak at 27.3°, which was indexed as {2 1 ½}, and its appearance was correlated with the $\langle L_C \rangle$ length. The magnetic, electric, and structural properties were governed by the axial lengths of nanorods. In practice, the memory capacity of $GdMn_2O_5$ nanorods can be calculated by minimizing their functional size by fabricating upstanding pillars with a cross-sectional area of 31 nm^2. Therefore, the estimated maximal capacity was approximately 650 Gbits/in^2.

Declaration of Competing Interest

The authors declare that they have no known competing financial interests or personal relationships that could have appeared to influence the work reported in this paper.

Acknowledgements

Supplementary materials

Supplementary material associated with this article can be found, in the online version, at doi:10.1016/j.cjph.2021.01.011.

Reference

[1] E. Ascher, H. Rieder, H. Schmid, H. Stössel, Some properties of ferromagnetoelectric Nickel-Iodine boracite, $Ni_3B_7O_{13}I$, J. Appl. Phys. 37 (1966) 1404.

[2] Hans Schmid, Multi-ferroic magnetoelectrics, Ferroelectrics 162 (1994) 317.

[3] Nicola A. Spaldin, Manfred Fiebig, The renaissance of magnetoelectric multiferroics, Science 309 (2005) 391.

[4] W. Eerenstein, N.D. Mathur, J.F. Scott, Multiferroic and magnetoelectric materials, Nature 442 (2006) 759.

[5] Nicola A. Spaldin, Sang-Wook Cheong, Ramamoorthy. Ramesh, Multiferroics: past, present, and future, Phys Today 63 (2010) 38.

[6] S.Y. Yang, F. Zavaliche, L. Mohaddes-Ardabili, V. Vaithyanathan, D.G. Schlom, Y.J. Lee, Y.H. Chu, M.P. Cruz, Q. Zhan, T. Zhao, R. Ramesh, Metalorganic chemical vapor deposition of lead-free ferroelectric $BiFeO_3$ films for memory applications, Appl. Phys. Lett. 87 (2005), 102903.

[7] H.T. Yi, T. Choi, S.-.W. Cheong, Reversible colossal resistance switching in (La,Pr,Ca)MnO_3: cryogenic nonvolatile memories, Appl. Phys. Lett. 95 (2009), 063509.

[8] Yu-Ting Tsai, Ting-Chang Chang, Wei-Li Huang, Chih-Wen Huang, Yong-En Syu, Shih-Cheng Chen, Simon M. Sze, Ming-Jinn Tsai, Tseung-Yuen Tseng, Investigation for coexistence of dual resistive switching characteristics in $DyMn_2O_5$ memory devices, Appl. Phys. Lett. 99 (2011), 092106.

[9] F. Zavaliche, T. Zhao, H. Zheng, F. Straub, M.P. Cruz, P.-.L. Yang, D. Hao, R. Ramesh, Electrically assisted magnetic recording in multiferroic nanostructures, Nano Lett 7 (2007) 1586.

[10] Manuel Bibes, Agnès Barthélémy, Towards a magnetoelectric memory, Nat Mater 7 (2008) 425.

[11] Charles Kittel, Theory of the Structure of ferromagnetic domains in films and small particles, Phys. Rev. 70 (1946) 965.

[12] S.N. Piramanayagam, Perpendicular recording media for hard disk drives, J. Appl. Phys. 102 (2007), 011301.

[13] N. Hur, S. Park, P.A. Sharma, J.S. Ahn, S. Guha, S.-.W. Cheong, Electric polarization reversal and memory in a multiferroic material induced by magnetic fields, Nature 429 (2004) 392.

[14] Hiroyuki Tsujino, Kay Kohn, Magnetoelectric effect of $GdMn_2O_5$ single crystal, Solid State Commun 83 (1992) 639.

[15] B.M. Kadomtseva, S.S. Krotov, Yu.F. Popov, G.P. Vorob'ev, Features of the magnetoelectric behavior of the family of multiferroics RMn_2O_5 at high magnetic fields, Low Temp. Phys. 32 (2006) 709.

[16] Jian-Tao Han, Yun-Hui Huang, Wei Huang, John B. Goodenough, Selective synthesis of $TbMn_2O_5$ nanorods and $TbMnO_3$ micron crystals, J. Am. Chem. Soc. 128 (2006) 14454.

[17] Gangqiang Zhu, Peng Liu, Mirabbos Hojamberdiev, Bao Ge, Yun Liu, Hongyan Miao, Guoqiang Tan, Synthesis RMn_2O_5 (R = Gd and Sm) nano- and microstructures by a simple hydrothermal method, Mater Chem Phys 118 (2009) 467.

[18] A.C. Larson, R.B. Von Dreele, General Structure Analysis System (GSAS), Los Alamos National Laboratory Report LAUR, 1994, pp. 86–748.

[19] See supplementary material Fig. S1.

[20] L.C. Chapon, G.R. Blake, M.J. Gutmann, S. Park, N. Hur, P.G. Radaelli, S.-.W. Cheong, Structural anomalies and multiferroic behavior in magnetically frustrated $TbMn_2O_5$, Phys. Rev. Lett. 93 (2004), 177402.

[21] See supplementary material Fig. S2.

[22] V. Skumryev, V. Laukhin, I. Fina, X. Martí, F. Sánchez, M. Gospodinov, J. Fontcuberta, Magnetization reversal by electric-field decoupling of magnetic and ferroelectric domain walls in multiferroic-based heterostructures, Phys. Rev. Lett. 106 (2011), 057206.

[23] M. Fiebig, Th. Lottermoser, D. Fröhlich, A.V. Goltsev, R.V. Pisarev, Observation of coupled magnetic and electric domains, Nature 419 (2002) 818.

[24] F. Kagawa, M. Mochizuki, Y. Onose, H. Murakawa, Y. Kaneko, N. Furukawa, Y. Tokura, Dynamics of multiferroic domain wall in spin-cycloidal ferroelectric $DyMnO_3$, Phys. Rev. Lett. 102 (2009), 057604.

[25] See supplementary material Fig. S3.

[26] Gianluca Giovannetti, Jeroen van den Brink, Electronic correlations decimate the ferroelectric polarization of multiferroic $HoMn_2O_5$, Phys. Rev. Lett. 100 (2008), 227603.